RSC Advances

ROYAL SOCIETY
OF CHEMISTRY

www.rsc.org/advances

RSC Advances

COMMUNICATION

Direct Evidence of Conversion Mechanism in NiSnO₃ Anode for Lithium Ion Battery Application

Lijun Fu,[b] †Kepeng Song,[d] †Xifei Li,[e] Peter A. van Aken,[d] Chunlei Wang, [*b,c] Joachim Maier[b] and Yan Yu [*a,b]

Recently, the ternary NiSnO₃ was first reported as an anode for Li-ion battery, presenting superior electrochemical performance to that of the NiO/SnO₂ mixture. This was proposed to be due to the 'self-matrix' function of the discharge products that enables buffering the volume change and preventing the aggregation upon cycling. In this article, direct evidence of the 'self-matrix' mechanism of NiSnO₃ has been observed via *ex-situ* transmission electron microscopy (TEM) and selected area electron diffraction (SAED).

The aim to achieve higher energy densities of lithium ion batteries triggered enormous research activities not only with respect to new materials, but also with respect to different lithium storage mechanisms, such as intercalation, phase transformation or conversion reaction[1]. In contrast to materials with intercalation and phase transformation mechanisms, such as graphite[2,3], LiCoO₂[4], LiFePO₄[5, 6], Li₄Ti₅O₁₂[7, 8], which offer limited structural space for lithium (de)intercalation, the materials with conversion reaction deliver higher capacity, by utilizing all oxidation states of transition metals, such as CoO[9], Cu₂O[9], Fe₂O₃[10], RuO₂[11]. However, these materials are far from being used commercially, intrinsically due to their large volume change during conversion reaction, large voltage hysteresis, low round-trip energy density loss and low coulombic efficiency, particularly in the first cycle [12].

Several strategies were reported to address these issues, especially for maintenance of the structural ability and hence the cycle performance, such as design of porous structured materials[13], and adding inactive[14] or active materials (e.g. carbon[15]) as a buffer matrix. However, either inactive or active addition as matrix would decrease the total energy density of the electrode, thus the advantage of conversion reaction would be less distinctive. Another strategy was to use mixed metal oxides containing two transition metals with a AB₂O₄ spinel structure, such as CoMn₂O₄[16], MFe₂O₄ (M = Zn, Co,

Ni)[17, 18], FeCo₂O₄[19-21], NiCo₂O₄[22, 23]. These spinels show a single plateau during the lithiation process due to mixed Femi level, which is different from the expected two individual reduction potentials. In the case of FeCo₂O₄[19], only a small plateau appears prior to the main reduction plateau during the first discharge, which is due to the formation of an intermediate CoO-like phase, while the spinel bond are still maintained confirmed by Infrared (IR) spectroscopy observation.
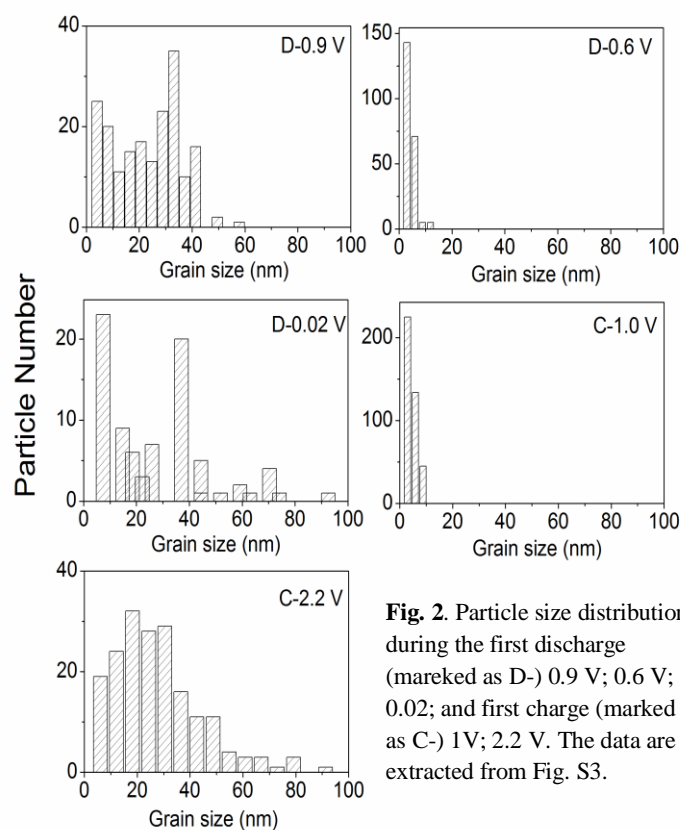
Recently, two of us demonstrated a nickel tin oxide (NiSnO₃, denoted as NSO) as a potential anode material for the lithium-ion battery[24]. Different from typical spinel mixed metal oxides, NSO presents multiple plateaus during the first lithiation process. Specific capacity and cycle performance of NSO are superior to that of simple mixture of NiO and SnO₂ (denoted as NAS). To explain this, a 'self-matrix' mechanism was suggested, according to which, the resultant discharge products after electrochem-decomposition act as buffer matrix for each other, alleviating the volume change and enhancing cycle performance without sacrificing specific capacity. However, direct evidence hasn't been obtained in our previous study. TEM is an attractive, efficient and powerful tool to detect structure and phase changes during the electrochemical conversion reaction[22]. Unlike simple oxides[25, 26], in convention reactions involving multiple cations[12], as here, it is significantly important to directly observe their structural changes during lithiation/delithiation *via* TEM.

Hereby, the reaction pathway of NiSnO₃ anode is observed via *ex-situ* SAED and TEM. We confirmed that the electrochemical decomposition of NiSnO₃ into NiO and Sn occurs during the first discharge process, followed by decomposition of NiO and Sn-Li alloying process. The initial decomposition products NiO and Sn act as the counter buffer matrix for each other, which enhance the electrochemical performance of NiSnO₃.
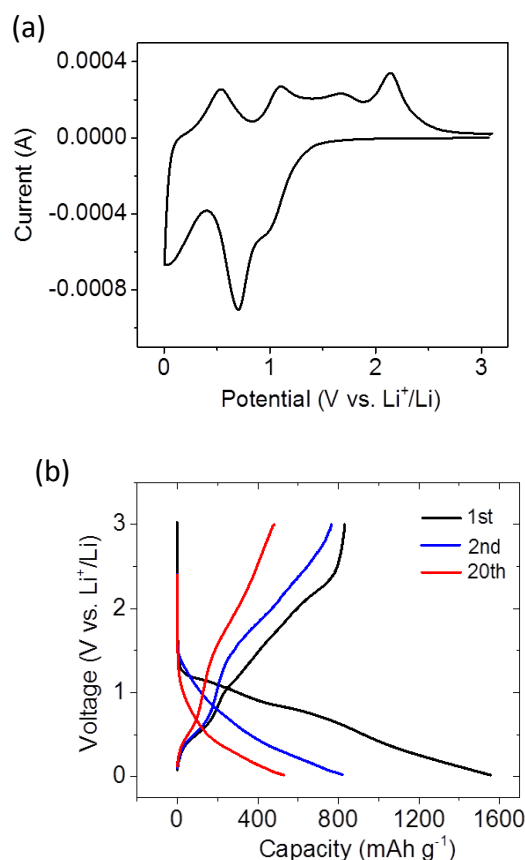
Fig. 1. (a) The cyclic voltammogram (first cycle) of NiSnO₃ at a scan rate of 0.1 mV s⁻¹; (b) The 1st , 2nd and 20th galvanostatic discharge/charge profiles of NiSnO₃ at a current density of 100 mA g⁻¹.

Fig. 2. Particle size distribution during the first discharge (mareked as D-) 0.9 V; 0.6 V; 0.02; and first charge (marked as C-) 1V; 2.2 V. The data are extracted from Fig. S3.

The X-ray diffraction (XRD) pattern of NiSnO₃ is shown in Fig. S1, which is in agreement with our previous result [24]. The particle size of NiSnO₃ is ranging from 50 to 100 nm, judging from the scanning electron microscopy (SEM) image (Fig. S2). The TEM images of NiSnO₃ are shown in Fig. S3a and S3b, the *d*-spacing values observed from high-resolution TEM are consistent with the XRD results. The results obtained from cyclic voltammetry (CV) shown in Fig. 1a indicates that at first cycle three peaks can be observed for the NiSnO₃ during the cathodic process, located around 1.0, 0.6 and 0 V vs. Li⁺/Li, corresponding to the reduction reaction of NiSnO₃ with lithium, while four peaks are located around 0.5, 1.0, 1.5 and 2.2 V in the anodic process, ascribed to the extraction of lithium from the discharge products. Consistent with the CV results, during the first discharge process of the galvanostatic charge-discharge measurement, the potential drops from 3 to 1.3 V vs. Li⁺/Li, followed by three plateau-like regimes, ranging from 1.3-0.9, 0.9-0.6 and 0.6-0 V, leading to a capacity of 1555 mAh g⁻¹. The charge process shows two distinguishable regimes ranging from 0-1 V and 1-2.2 V. The first charge capacity is 832 mAh g⁻¹ (Fig. 1b). Compared to the first discharge profile, the second discharge profile shows relatively lower lithiation potential, while the charge profiles of the following cycles are pretty similar to the first charge cycle,

with small polarization, indicating a similar de-lithiation process. The 20th charge-discharge profile is similar to that of the 2nd cycle, yet with capacity fading. The discharge-charge capacities at 20th cycle are 527 and 480 mAh g⁻¹, respectively.
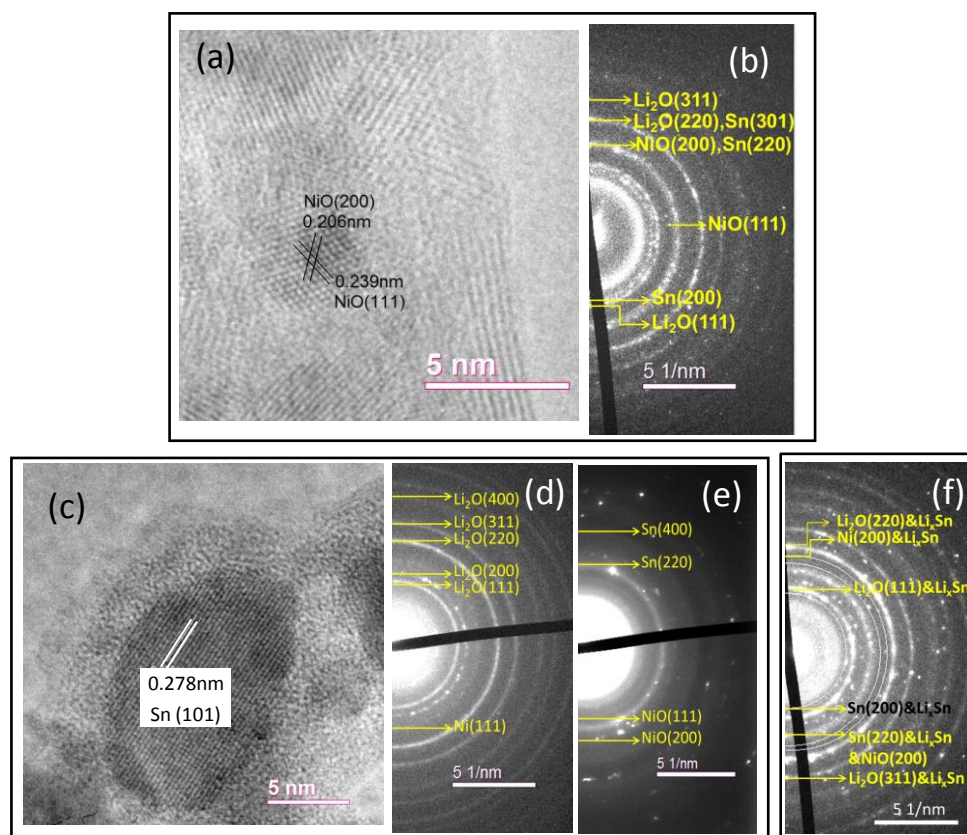
The discharge and charge products at different states of discharge (SODs) and charge (SOCs) were examined by bright-field TEM (Fig. S3c-S3g). Since NiSnO₃ shows a unique feature during its first discharge process, i.e., exhibiting multiple reduction plateaus rather than one (Fig. 1), compared to other mixed transition metal oxides [16-22], it is essential to understand the reaction pathway of its first reduction process. When discharged NiSnO₃ to 0.9 V, particles with two main size distributions are observed, i.e., bimodal distribution, ~ 5 and ~ 30 nm (Fig. 2 and S3c, typical particles are marked with yellow and red circles, respectively). With the increase of state of discharge (SOD) to 0.6 V, a remarkable decrease of particle size to less than 5 nm can be observed, which indicates a further decomposition of discharge products (Fig. 2 and S3d). In contrast, when discharging to 0.02 V, the particle size increases (Fig. 2 and S3e). At the meantime, some of the particles remaining its small particle size can be observed as depicted with brown circles in Fig. S3e, which can play a role as volume buffer during the alloying procedure. The morphologies of charge products at different SOCs have also been examined by bright-field (BF) TEM imaging. When charging up to 1.0 V, the particle size of the sample is 5-10 nm (Fig. 2 and S3f), and decreases dramatically compared with that of at 0.02 V. At 2.2 V, the particle size of the part of the products increased to be 40-100 nm (Fig. 2 and S3g). The primary TEM observation, especially change of particle size, indicates that NiSnO₃ experiences

an electrochemically milling process during the first discharge process. For detailed information, SAED and HRTEM are applied for further investigation.
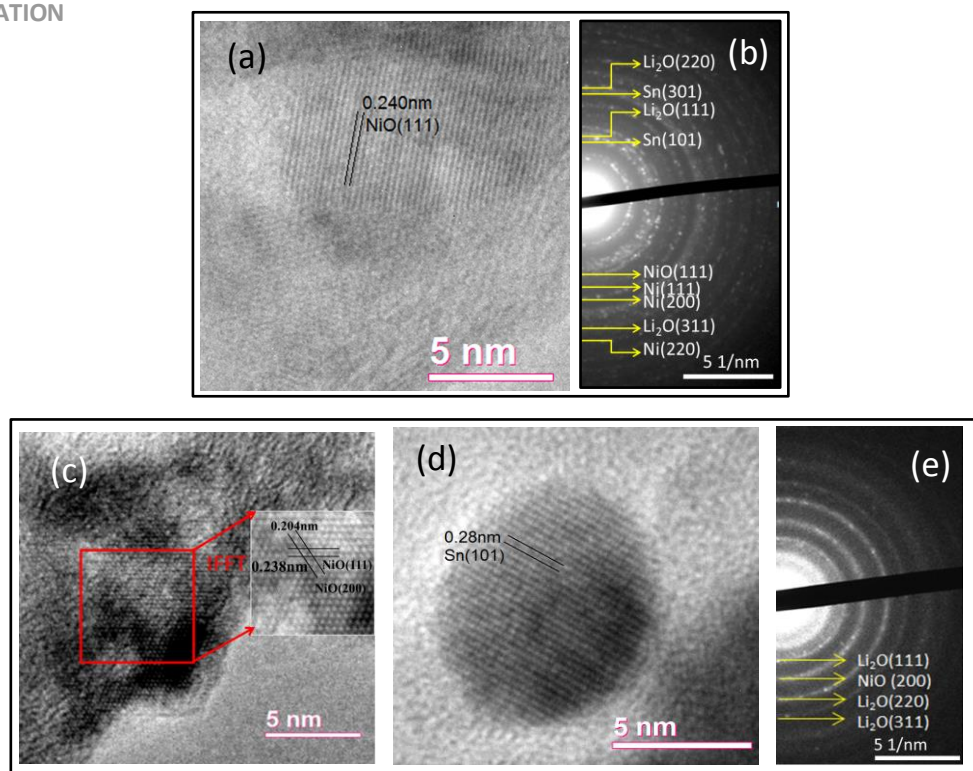
The SAED patterns of discharge and charge products during the first cycle at different SODs and SOCs are shown in Fig. 3 and Fig. 4. Since the high-resolution TEM (HRTEM) images of products at different potentials during the first cycle show only a low grade of crystallinity, which usually gets better during cycling [27], the HRTEM images of reaction products for the 20th cycle were examined for comparison. The SAED patterns of the reduced product at 0.9 V in the 1st cycle (Fig. 3b) show the polycrystalline nanostructures of the sample with multiple concentric rings which can be ascribed to Sn (200), (220), (301), Li$_2$O (111) (220) (311) and NiO (200) (111). The correlated d-spacing values of each substance are shown in Table S2. Overlap of the rings can be observed from the SAED pattern, while the representative diffraction rings of NiO (111), Sn (200) and Li$_2$O (111) confirm that when discharging NiSnO$_3$ to 0.9 V, it decomposes into Sn, NiO and Li$_2$O. The HRTEM images of the discharged products at 0.9 V for the 20th cycle demonstrate the existence of NiO in the composites with typical lattice d-spacing of NiO (200) (111), as shown in Fig. 3a. For the discharge products at 0.6 V in the 1st cycle, the SAED patterns (Fig. 3d and 3e) reveal that beside the existence of Li$_2$O, Sn and NiO, Ni metal is also appearing in the resulted products after discharging NiSnO$_3$ to 0.6 V, indicating a decomposition of NiO to Ni and Li$_2$O upon lithium intercalation occurs at the potential of 0.6 V. However, the decomposition is not complete since there is still remaining NiO in the nanocomposites. The HRTEM image of the discharge product at 0.6 V for 20th cycle shows a clear existence of Sn particle with a particle size of ~ 10 nm (Fig. 3c). When discharging NiSnO$_3$ to 0.02 V, the particle size of the discharged product increases, together with the fact that there is no alloy reaction between lithium and nickel [28], the cathodic peak around 0 V (slope regime below 0.5 V in first discharge profile, Fig. 1) is mainly ascribed to lithium-tin alloy (Table S1). The SAED patterns show that the resulting nanocomposite exhibit a polycrystalline nanostructure (Fig. 3f), the SAED circles of Sn, Ni, NiO, Li$_2$O in the SAED pattern are overlapped with those of Li$_x$Sn[29], which makes it difficult to identify the separate phases.

For the charge process, consider the similarity of the de-lithiation process between first and following cycles [24] (Fig. 1b), the charge products between 1st and 20th cycles are comparable in terms of components. When charging to 1.0 V, the particle size shrinks (Fig. 2), indicating a de-lithiation process of Li-Sn alloy, which is consistent with the previous reports (Table S1). The SAED patterns at 1.0 V (Fig. 4b) present the typical diffraction rings of Ni (111) (200) (220), NiO (111), Sn (101) (301) and Li$_2$O (111) (220) (311), confirming that the charged nanocomposites at 1.0 V contain Ni, NiO, Sn and Li$_2$O. HRTEM images show the d-spacing value of 0.240 nm, which should be corresponding to the crystal lattice of NiO (111) (Fig. 4a). The NiO results from the incomplete conversion reaction during the discharge process. When charging up to 2.2 V, the SAED patterns reveal that the resulted nanocomposite consists of

Fig. 3. HRTEM of discharge products at different SODs after 20 cycles (a) 0.9 V; (c) 0.6 V; and SAED patterns of discharge products at different SODs during the first discharge process (b) 0.9 V; (d-e) 0.6 V; (f) 0.02 V.
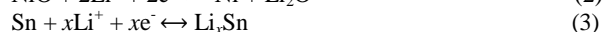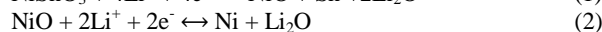
Fig. 4. HRTEM of charge products at different SOCs after 20 cycles (a) 1V; (c-d) 2.2 V and SAED patterns of charge products at different SOCs during the first discharge process (b) 1 V; (e) 2.2 V.

NiO and Li_2O (Fig. 4e). HRTEM image (Fig. 4d) of samples charge up to 2.2 V after 20 cycles show clearly the crystal lattice of Sn (101), besides, the crystal lattice of NiO (111) and (200) can be observed via the inverse fast Fourier transform (IFFT) (Fig. 4c). It confirms that when charging up to 2.2 V, the nanocomposites contain NiO, Sn and Li_2O.

**Table 1.** Discharge/charge products at different SOD/SOC during the first cycle.

Products at different SOD/SOC	Li_2O	Li_xSn	Sn	NiO	Ni
0.9 V	✓		✓	✓	
0.6 V	✓		✓	✓	✓
0.02 V	✓	✓	--	✓	✓
1.0 V	✓	✓	✓	✓	
2.2 V	✓		✓	✓	

From the TEM and SAED results, the components of the reduction products at different SODs and SOCs are listed in Table 1. The conversion reaction mechanism of $NiSnO_3$ can be confirmed and illustrated in Scheme 1 and Eq. (1-3):

$$NiSnO_3 + 4Li^+ + 4e^- \longrightarrow NiO + Sn + 2Li_2O \qquad (1)$$
$$NiO + 2Li^+ + 2e^- \longleftrightarrow Ni + Li_2O \qquad (2)$$
$$Sn + xLi^+ + xe^- \longleftrightarrow Li_xSn \qquad (3)$$

During the first discharge process, $NiSnO_3$ is electrochemically decomposed into NiO, Sn and Li_2O (Discharge 1, 0.9 V), followed by the decomposition of NiO into Ni / Li_2O nanocomposites (Discharge 2, 0.6 V), and lithium alloying with Sn (Discharge 3, 0.02 V), the appearance of Sn can not be clearly identified, due to the overlap of diffraction rings of Li_xSn and Sn. In the charge process, Li_xSn is dealloyed first when the potential is below 1.0 V (Charge 1), when charging up to 2.2 V, Ni metal is oxidized and NiO is reformed (Charge 2). This is different from our previous hypothesis of the charge process (marked with dashed arrow in Scheme 1) [24]. The decomposition of NiO is not completed during the discharge process, thus the NiO appears in each of the following step (Scheme 1 and Table 1). This reaction pathway can also explain the particle size changes of the discharge/charge products shown in Fig. 2. For the product at 0.9 V, the particles with a particle size of ~ 5 nm are supposed to be Sn nanoparticles and those with a size of ~ 30 nm might be NiO (Fig. S3c), which then decomposes further into much smaller particles Ni and Li_2O (~ 5 nm) during the further reduction, observed in Fig. S3d. The expansion and shrinkage of particles at 0.02 V (Fig. S3e) and 1V (Fig. S3f) are mainly due to the alloying/de-alloying process of Sn, respectively. The charged products at 2.2 V are NiO, Sn and Li_2O. Similar as the other ternary spinel oxides [16-22], the reformation of $NiSnO_3$ is not realized. This could explain the difference of discharge/charge profile between the first and following cycles (Fig. 1b), in which the decomposition of NiO occurs at ~ 1.2 V (Table 1) [30]. The incomplete decomposition of NiO results in the capacity fading during cycling, in spite of the superior capacity retention ability of NSO to NAS. Compared to NAS, the distribution of the electrochemical production of NSO (NiO and Sn) during the first cycle is more homogeneous (Fig. S4 and S5), resulting in better 'self-matrix' buffer function and electrochemical performance [24].
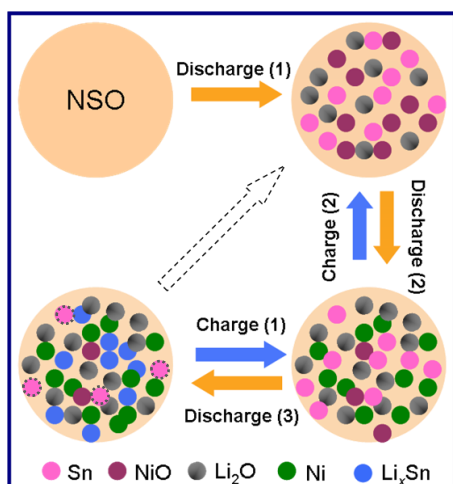
Scheme 1 Conversion reaction mechanism of NiSnO$_3$ anode as 'self-matrix' in lithium ion batteries; the dashed arrow indicates the demonstration of charge process in our previous report [24]. (The dash circle around Sn particles shows the possibility of Sn in the discharged product at 0.02 V).

Conclusions

In conclusion, the conversion reaction mechanism of NiSnO$_3$ has been studied via TEM and SAED methods. Different from other mixed transition metal oxides, NiSnO$_3$ exhibits multiple reduction plateaus during its initial discharge process, which are due to the decomposition of NiSnO$_3$ and formation of NiO, Sn and Li$_2$O at 0.9 V, decomposition of NiO at 0.6 V, and followed by the alloy process of Sn. Opposite reaction pathway is confirmed during charge process, and results in NiO and Sn as the products when charge up to 2.2 V. The electrochemically formed NiO and Sn during the first discharge process can act as 'self-matrix' buffer for each other during the subsequent reactions, besides the widely recognized buffer effect from Li$_2$O, resulting in superior energy density and better cycle performance, compared to the bare nanocomposites of NiO and SnO$_2$ (NAS). However, incomplete reaction of NiO during discharge could be the main reason for the slow degradation of the storage capacity. Replacement of the commercial NiSnO$_3$ with a sample controlled porosity and size distribution could further improve its cycling performance.

Acknowledgements

Notes and references

^{a} School of Chemistry and Materials Science, University of Science and Technology of China, Hefei, China.. Tel: 86- 551-63607179; E-mail: yanyumse@ustc.edu.cn.

^{b}Max Planck Institute for Solid State Research, Heisenbergstr. 1, Stuttgart, 70569, Germany. Fax:49-7116891722; Tel:49-7116891725;

^{c}Department of Mechanical and Materials Engineering, Florid, International University Miami, FL 33174, USA. E-mail: wangc@fiu.edu.

^{d}Max Planck Institute for Intelligent Systems, Heisenbergstr. 3, Stuttgart, 70569, Germany
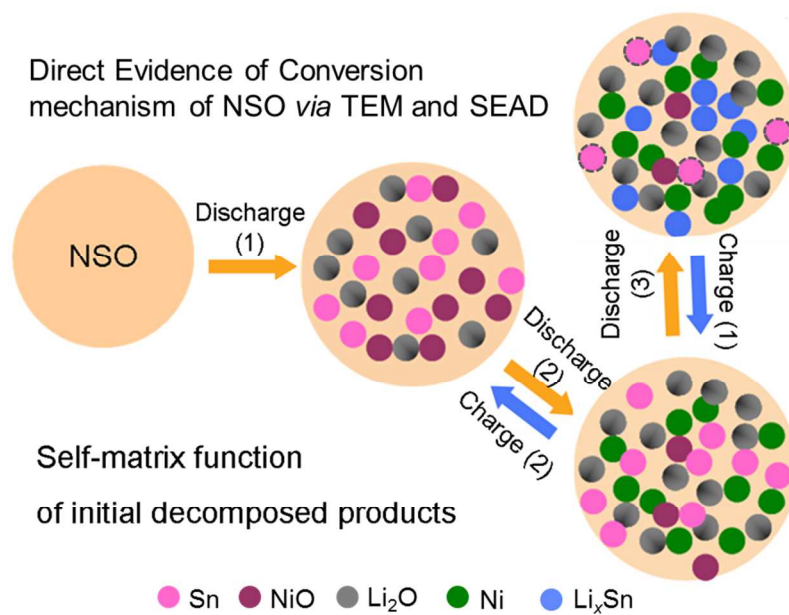
^{e}Department of Engineering, The University of Western Ontario, London, Ontario, Canada, N6A 5B9

† Dr. Lijun Fu and Mr. Kepeng Song contributed equally to this work.

† Electronic Supplementary Information (ESI) available: [Experimental section, XRD patterns of NiSnO$_3$, SEM image of NiSnO$_3$ before cycling, Assignment of redox peaks of NiO and Sn during reactions with lithium, Assignment of the Bragg reflections based on d-values for Sn, Li$_2$O, Ni, and NiO from SEAD patterns]. See DOI: 10.1039/c000000x/

1. M. S. Whittingham, *Chem. Rev.*, 2004, **104**, 4271-4302.
2. M. Winter, J. O. Besenhard, M. E. Spahr and P. Novák, *Adv. Mater.*, 1998, **10**, 725-763.
3. N. A. Kaskhedikar and J. Maier, *Adv. Mater.*, 2009, **21**, 2664-2680.
4. K. Mizushima, P. C. Jones, P. J. Wiseman and J. B. Goodenough, *Mater. Res. Bull.*, 1980, **15**, 783-789.
5. A. K. Padhi, K. S. Nanjundaswamy and J. B. Goodenough, *J. Electrochem. Soc.*, 1997, **144**, 1188-1194.
6. C. Zhu, Y. Yu, L. Gu, K. Weichert and J. Maier, *Angew. Chem. Inter. Ed.*, 2011, **50**, 6278-6282.
7. E. Ferg, R. J. Gummow, A. de Kock and M. M. Thackeray, *J. Electrochem. Soc.*, 1994, **141**, L147-L150.
8. L. Yu, H. B. Wu and X. W. Lou, *Adv. Mater.*, 2013, 2296-2300.
9. P. Poizot, S. Laruelle, S. Grugeon, L. Dupont and J. M. Tarascon, *Nature*, 2000, **407**, 496-499.
10. N. A. Godshall, I. D. Raistrick and R. A. Huggins, *Mater. Res. Bull.*, 1980, **15**, 561-570.
11. P. Balaya, H. Li, L. Kienle and J. Maier, *Adv. Funct. Mater.*, 2003, **13**, 621-625.
12. J. Cabana, L. Monconduit, D. Larcher and M. R. Palacín, *Adv. Mater.*, 2010, **22**, E170-E192.
13. Y. Yu, L. Gu, A. Dhanabalan, C.-H. Chen and C. Wang, *Electrochim. Acta*, 2009, **54**, 7227-7230.
14. X. Li, A. Dhanabalan and C. Wang, *J. Power Sources*, 2011, **196**, 9625-9630.
15. S.-H. Lee, V. Sridhar, J.-H. Jung, K. Karthikeyan, Y.-S. Lee, R. Mukherjee, N. Koratkar and I.-K. Oh, *ACS Nano*, 2013.
16. P. Lavela, J. L. Tirado and C. Vidal-Abarca, *Electrochim. Acta*, 2007, **52**, 7986-7995.
17. S. Ren, X. Zhao, R. Chen and M. Fichtner, *J. Power Sources*, 2014, **260**, 205-210.
18. N. Wang, H. Xu, L. Chen, X. Gu, J. Yang and Y. Qian, *J. Power Sources*, 2014, **247**, 163-169.

19. P. Lavela, G. F. Ortiz, J. L. Tirado, E. Zhecheva, R. Stoyanova and S. Ivanova, *The J. Phys. Chem. C*, 2007, **111**, 14238-14246.

20. Y. Sharma, N. Sharma, G. V. Subba Rao and B. V. R. Chowdari, *Solid State Ionics*, 2008, **179**, 587-597.

21. Y.-Q. Chu, Z.-W. Fu and Q.-Z. Qin, *Electrochim. Acta*, 2004, **49**, 4915-4921.

22. Y. NuLi, P. Zhang, Z. Guo, H. Liu and J. Yang, *Electrochem. Solid-State Lett.*, 2008, **11**, A64-A67.

23. L. Shen, Q. Che, H. Li and X. Zhang, *Adv. Funct. Mater.*, 2014, **24**, 2630-2637.

24. X. Li and C. Wang, *RSC Adv.*, 2012, **2**, 6150-6154.

25. S. Grugeon, S. Laruelle, R. Herrera-Urbina, L. Dupont, P. Poizot and J.-M. Tarascon, *J. Electrochem. Soc.*, 2001, **148**, A285-A292.

26. X. W. Guo, X. P. Fang, Y. Sun, L. Y. Shen, Z. X. Wang and L. Q. Chen, *J. Power Sources*, 2013, **226**, 75-81.

27. Y. Yu, Y. Shi, C.-H. Chen and C. Wang, *J. Phys. Chem. C*, 2008, **112**, 4176-4179.

28. J. Zhao, Q. Y. Gao, C. Gu and Y. Yang, *Chem. Phys. Lett.*, 2002, **358**, 77-82.

29. G. R. Goward, N. J. Taylor, D. C. S. Souza and L. F. Nazar, *J. Alloys Comp.*, 2001, **329**, 82-91.

30. X. H. Huang, J. P. Tu, B. Zhang, C. Q. Zhang, Y. Li, Y. F. Yuan and H. M. Wu, *J. Power Sources*, 2006, **161**, 541-544.

Direct Evidence of Conversion mechanism of NSO *via* TEM and SEAD

Self-matrix function of initial decomposed products

Discharge (1)

Discharge (2)

Charge (2)

Discharge (3)

Charge (1)

NSO

● Sn   ● NiO   ● Li_2O ● Ni   ● Li_xSn

'Self-matrix' function of $NiSnO_3$ as anode in Li-ion battery has been investigated via *ex-situ* TEM and SAED.